Sensitivity and reproducibility of Transverse Magneto-Optical Kerr Effect (T-MOKE) ellipsometry

Carmen Martín Valderrama[1], Mikel Quintana[1], Ane Martínez-de-Guerenu[2,3], Tomoki Yamauchi[4], Yuki Hamada[4], Yuichiro Kurokawa[4], Hiromi Yuasa[4] and Andreas Berger[1]

[1]CIC nanoGUNE BRTA, Tolosa Hiribidea 76, E-20018 Donostia—San Sebastián, Spain

[2] CEIT-Basque Research and Technology Alliance (BRTA), Manuel Lardizabal 15, E-20018 Donostia—San Sebastián, Spain

[3] Universidad de Navarra, Tecnun, Manuel Lardizabal 13, E-20018 Donostia—San Sebastián, Spain

[4]Graduate School and Faculty of Information Science and Electrical Engineering, Kyushu University, Fukuoka 819-0395, Japan

Abstract

We report a comprehensive experimental study to analyze the limiting factors and physical mechanisms that determine the achievable performance of Transverse Magneto-Optical Kerr Effect (T-MOKE) ellipsometry. Specifically, we explore different approaches to achieve high sensitivity and reduced acquisition times. The best sensitivity is observed for an incident light polarization with balanced s-p components. We also verify experimentally that the method's theoretical description is accurately describing data for any s-p combination of the incoming light. Furthermore, two alternative measurement strategies are explored by using different measurement sequences for the polarization sensitive optics, which both achieve a very comparable, high quality of results. Signal-to-noise ratios and systematic deviations are measured and analyzed based on a large number of nominally identical measurement repeats, both for entire signal sequences as well as for individual Fourier components of the magneto-optical signal generated by a sinusoidal magnetic field sequence. Hereby, we observe that while higher order Fourier components have a significantly reduced signal amplitude and correspondingly exhibit reduced signal-to-noise and repeatability performance, signal-to-noise ratios always exceed values of 100 even for the lowest signal Fourier component and the lowest signal sample that we investigated, illustrating the extremely precise nature of T-MOKE ellipsometry.

1. Introduction

Understanding magnetic phenomena is a subject of immense scientific research activity because of the numerous technological applications of magnetism and magnetic materials in devices [1-4]. Therefore, cutting edge analytic tools for the characterization of magnetic properties of advanced materials are needed to further improve our knowledge of magnetism, associated materials and device components. A large variety of techniques has been developed, which include techniques based on X-ray magnetic dichroism [5] or magneto-optical effects [6, 7]. Magneto-optical based techniques in particular are very sensitive to detect magnetism by widely applicable and cost-effective experimental set-ups [8, 9]. Also, Magneto-Optical Kerr Effect (MOKE) techniques can be used to probe a sample's magnetism locally, image it, and extract information about magnetic configurations and reversal processes by analyzing the signal or images obtained in such measurements [10-12]. MOKE techniques have been demonstrated to be especially useful for materials characterization and the study of the magnetization properties in thin films, surfaces, and layered structures [13-15]. Furthermore, magneto-optical effects have not only been used as characterization techniques for magnetization properties [16, 17] but also for ultra-fast magnetization dynamics detection [18, 19] and spintronic process and device measurements [2, 19]. Moreover, optical isolation and modulation devices [21, 22], magnetoplasmonics [23, 24], data storage technologies [3, 25] and bio-sensing [26, 27], among other fields [28-31], utilize magneto-optical effects.

MOKE effects are most-commonly classified according to the geometry of the magnetization direction with respect to the sample surface and the plane-of-incidence of the light beam. Figure 1 shows a schematic of our particular MOKE set-up, as well as the overall measurement procedure. In figure 1(a), the sample surface is represented by the grey surface and the plane-of-incidence is the plane defined by combining the incoming and reflected light beam. The polar MOKE (P-MOKE) effect is generated by the magnetization vector component perpendicular to the sample surface, and longitudinal and transverse MOKE (L-MOKE and T-MOKE) effects are associated with the magnetization vector components contained in the surface plane of the sample, and are, respectively, parallel to the plane-of-incidence and perpendicular to it [15, 32]. In the case of P- and L-MOKE, the sample magnetization leads to a

rotation and ellipticity change of the reflected light polarization for incoming s- or p-polarized light, an effect that inverts if the magnetization itself is inverted. For T-MOKE, one observes a change in the amplitude or intensity of the reflected light for incident p-polarized radiation, which is also reversed upon magnetization reversal [14]. Moreover, there are magneto-optical effects that depend on the magnetization vector components in higher order, which are also well described in the literature [33-36].

The MOKE geometry used in the present work is the transverse geometry. Conventionally, T-MOKE experiments are simpler as they can be performed as mere intensity measurements. Another and even more relevant advantage of T-MOKE experiments is the experimental geometry of the set-up, because it allows for a more flexible design due to the spatial separation of the optical elements from the magnetic field generating components, which are arranged in perpendicular planes [37]. In the pure intensity measurement mode, T-MOKE usually produces weaker signal amplitudes than L- and P-MOKE [38, 39], but previous works have demonstrated that with the effective polarization detection measurement scheme [37, 40], the sensitivity of T-MOKE measurements can be improved significantly and made comparable to L-MOKE measurements [37, 40].

The already mentioned pure intensity measurement mode, which is the conventional T-MOKE method, uses only p-polarized light and light intensity changes are measured as the sample magnetization is changed. The effective polarization T-MOKE method [40] uses a mixture of s- and p-polarized light for the incident light beam. As T-MOKE produces a change in the intensity of the reflected light only for incident p-polarized radiation, the s-polarized component is not affected by the T-MOKE effect. The associated modification of amplitude and phase of only one of the reflected light components results in a net polarization change in the reflected light, as long as the incoming light is not pure s- or p-polarization. Therefore, T-MOKE measurements can be performed as polarization measurements. An additional improvement of the sensitivity has been achieved via an ellipsometric approach [37]. Hereby, the ellipse that represents the polarization state of the reflected light is determined, so that the relative change in polarization can be measured with very high accuracy. Moreover, the magneto-optical polarization modification is superimposed onto purely optical polarization modifications, so that both optical

and magneto-optical effects can be accurately measured [37]. For T-MOKE ellipsometry measurements, the effective polarization detection conditions are changed during the measurement sequence, and in conjunction with the corresponding data analysis, this method was demonstrated to be able to obtain full magneto-optical and optical sample information, as well as isolate noise and false background signals. Key experimental aspects of this T-MOKE ellipsometry method were already discussed in [37].

While prior T-MOKE ellipsometry works demonstrated the overall potential of the methodology, they did not systematically analyze the achievable performance levels and more importantly, they did not identify the leading noise sources and physical mechanisms that control the methodologies performance levels. This is particularly relevant in relation to three key experimental conditions that must be selected for any T-MOKE ellipsometry measurement, which are: the incoming light polarization, the selected grid of measurement settings, and the re-combination of frequency filtered signal pattern that are being utilized for efficient noise filtering. Without detailed knowledge of these aspects, an adequate utilization and adaptation of T-MOKE ellipsometry to specific sample and noise condition is not truly feasible. Therefore, the present work explores these crucial experimental aspects and overall, aims to understand the achievable sensitivity of T-MOKE ellipsometry by precisely characterizing the achieved signal and signal-to-noise ratios in detail, and explore the physical origins of the noise levels to understand fundamental and practical limits of this methodology. To achieve these goals, our comprehensive study of T-MOKE ellipsometry is conducted by using three separate experimental approaches, which are each described in their own respective results sections: (i) the best operational point is determined by analyzing the impact of the polarization angle of the incident light; (ii) given that different Fourier components of the total measured signal pattern can provide different information [17], a comparative study of their individual sensitivities and signal-to-noise performances is conducted; and (iii) a search for an improved experimental measurement sequence has been performed to explore another pathway of obtaining either higher sensitivity and/or reduced measurement times, similar to work conducted towards the optimization of the Generalized Magneto-optical Ellipsometry (GME) method [41]. Moreover, the quality and reproducibility of the T-MOKE ellipsometry data is analyzed in precise detail by repeating the

same type of measurement 100 times under identical conditions and quantitatively analyze deviations of each individual measurement from the average.

2. Experimental aspects

a. Experimental set-up

The specific set-up used in our study is schematically represented in figure 1(a). Following the light path represented by the red line from left to right, the set-up contains an ultra-low-noise solid-state laser producing light with wavelength λ = 635 nm and an output power of 5 mW [1], which is positioned in such a way that the laser light has an angle of incidence of 60º with respect to the surface normal of the sample. The incoming laser light passes first through a first linear polarizer P_1, which can be rotated in order to define the polarization axis of the incident light, given by angle θ_1. The orientation and the degree of linear polarization of the incident light is determined by P_1, even if the laser itself already produces linearly polarized light. However, the polarization ratio, which is the ratio in between the desired and the unwanted polarization orientation, is only of the order of about 100 for our laser, whereas this ratio improves to better than 100000 by using a dedicated polarizer, an aspect that is very significant, given that magneto-optical polarization changes are typically very small. The so-produced linear polarized light is then reflected by the sample, which is placed inside the gap of an electromagnet that applies a magnetic field along the transverse orientation (into the depth of the picture). On the reflected light arm, the light beam passes through a rotatable quarter wave plate QWP and a second rotatable linear polarized P_2, for the purpose of achieving detection conditions that allow for a sensitive polarization analysis[2]. The orientations of these optical elements are given by angles ϕ_2

[1] The laser used in these experiments is a Coherent ultra-low-noise laser, model ULN 635 nm; it has a wavelength of λ = 635 nm, a polarization ratio larger than 100:1, and an output power of 5 mW. A special modulation is used to force the laser into a multi-longitudinal mode, the result of which is low RMS noise (0.06%), which is stable over changes in temperature and the life of the laser module.

[2] The three polarization optics elements are a Zero-Order Quarter-Wave Plate that is fabricated by combining two Multi-Order Crystalline Quartz Wave Plates to obtain an optical path length difference of precisely λ/4, and two Nanoparticle Linear Film Polarizers consisting of prolate ellipsoid nanoparticles that have been embedded in sodium-silicate glass. Their spectral characteristic is such that polarization ratios better than 100000 are achieved for λ = 635 nm.

and θ_2, respectively. Finally, the transmitted light intensity *I* is measured with a Si-photodiode detector that includes a low noise, low offset, high gain on-chip amplifier[3]. The angles of the optical elements (θ_1, ϕ_2 and θ_2) are defined as the angle of their principal axis with respect to the s-polarization orientation, and positive values are associated with the counter-clockwise rotation sense along the light propagation direction, as indicated in figure 1(a) by the blue arrows. The two optical devices of the reflected light arm (QWP and P_2) are controlled in their orientation by precision motors that enable angle variations down to $2 \cdot 10^{-4}$ deg; the first polarizer P_1 can be rotated precisely by a manual rotation stage.

It is worthwhile to mention that our set-up does not utilize any light chopper or polarization modulation, which are approaches that have been used very successfully in the past by other groups [42]. Hereby, it is important to realize that the especially useful applications of such modulation techniques were realized for rather noisy light sources, in particular broad-band white light sources that were subsequently wavelength separated, leading to very low and fluctuating light levels. In contrast to this situation, our extremely stable laser source in conjunction with a mechanically very sturdy experimental set-up generates a very high signal-to-noise ratio of our measurements, even in DC-mode. Thus, an additional polarization modulation can actually lead to a reduction of the overall signal-to-noise ratio, given that any added element actually adds noise to an experiment. So, in contrast to these prior optical modulation approaches, we do not modulate the optical conditions of our experiment, but instead use a Fourier analysis of the field response as discussed below to optimize our experimental performance.

In the most general case, an absolute phase shift occurs in between s- and p-polarized light upon reflection, leading to elliptically polarized light, meaning that the temporal evolution of the electric field vector of the reflected light can be described by an ellipse. This change in the polarization state is used in conventional ellipsometry for the determination of optical constants and/or layer structures of the material under investigation. Upon appropriately aligning the

[3] Our photodetector is a Si Switchable Gain Detector designed for the wavelength range of 350 - 1100 nm and a band width of 12 MHz.

orientation of the QWP and P_2, extinction of this reflected light can be achieved at a particular setting, which is the so-called extinction point.

Moreover, for a magnetized sample, an additional modification to the polarization state of the reflected light appears. This additional change is dependent on the magnetization state, so that it can be well distinguished from the polarization change due to pure optical effects. Mathematically, both effects are most-commonly described in a quantitatively accurate manner by the reflection matrix

$$\underline{R} = \begin{pmatrix} r_s & \alpha + \gamma \\ -\alpha + \gamma & r_p + \beta \end{pmatrix} = r_p \begin{pmatrix} \tilde{r}_s & \tilde{\alpha} + \tilde{\gamma} \\ -\tilde{\alpha} + \tilde{\gamma} & 1 + \tilde{\beta} \end{pmatrix}, \quad (1)$$

utilizing the Jones calculus of polarization optics and containing the complex Fresnel coefficients r_s and r_p for s- and p-polarization, as well as the complex magneto-optical parameters α, β and γ which represent L-, T- and P-MOKE. The amplitudes of the magneto-optical parameters α, β and γ are much smaller than the amplitudes of the pure optical parameters r_s and r_p. As identified by equation (1), the parameters $\tilde{r}_s, \tilde{\alpha}, \tilde{\beta}$ and $\tilde{\gamma}$ are equal to r_s, α, β and γ, respectively, divided by r_p. The magneto-optical parameters of the reflection matrix are directly related with the magnetization $\vec{m}$ of the sample; $\alpha(\vec{m})$, $\beta(\vec{m})$ and $\gamma(\vec{m})$ will change their sign upon magnetization inversion: $\alpha, \beta, \gamma(-\vec{m}) = -\alpha, \beta, \gamma(\vec{m})$. As a consequence, the polarization state of the reflected light will be modified upon magnetization reversal.

In the transverse geometry of our experimental set-up, the applied magnetic field is parallel to the sample plane and perpendicular to the plane of incidence. Therefore, α and γ are equal to zero, so that the reflection matrix $\underline{R}$ has no off-diagonal components. Instead, the magneto-optical signal in our experimental set-up comes from the magneto-optical parameter β only. The magneto-optical signals for this specific case are related with changes in the ellipse of the reflected light associated to magnetization reversal induced variations of the phase and amplitude of the p-polarized component of the incident radiation.

The fundamental idea of T-MOKE ellipsometry is to utilize the interference of the purely optically induced ellipticity with the magnetically produced light polarization changes to determine both the magneto-optical and the pure optical elements of the reflection matrix and achieve a complete experimental characterization. In our measurements, the polarization of the incoming light is initially fixed by a defined orientation of P_1, which defines the s- and p-polarized components of the incident light. After locating the sample dependent light extinction point by varying θ_2 and ϕ_2, we use multiple settings of θ_2 and ϕ_2 in order to achieve different interference conditions for optics and magneto-optics, which allows us to determine the entire reflection matrix $\underline{R}$. Our prior work has shown that near the extinction point, one is extremely sensitive to the small magneto-optical effects [37, 40]. Specifically, we run a grid of QWP and P_2 settings to collect a complete T-MOKE ellipsometry data set. In a typical measurement sequence, the grid we use covers 21 x 21 (θ_2, ϕ_2) settings in an angular range of $\pm$4º away from the extinction point.

As can be seen in figure 1(b), we apply a sinusoidal magnetic field of frequency ω using an amplitude that is sufficient to invert the sample magnetization and achieve a magnetically saturated state along the field direction to facilitate an easy subsequent data interpretation. For the applied magnetic field of figure 1(b), the intensity detected at the photodetector for one particular setting of the optical elements is shown as a grey line in figure 1(c), exhibiting a near square-type signal trace. The detected time-dependent signal $I(t)$ is then filtered by means of a Fourier transformation and reconstructed by using only the field-synchronous amplitudes of the Fourier spectrum, i.e. signal components representing the fundamental frequency ω and its odd higher harmonics. The blue line in figure 1(c) represents the signal reconstructed from the amplitudes of the extracted odd Fourier components, which is virtually identical to the original signal, so that a Fourier transformation of the recorded I vs. t signal trace in conjunction with a frequency selected inverted Fourier transformations allows for efficient signal filtering and noise reduction [37]. The signal amplitude ΔI that is representative of the magnetization inversion effect onto the optical signal, i.e. the magneto-optical effect, is subsequently calculated as $\Delta I = 2(A_\omega - A_{3\omega} + A_{5\omega} - A_{7\omega})$, with $A_{i\omega}$ being the i^{th} order amplitude of the Fourier series, defined as a positive number. Higher order components than the 7^{th} order of the fundamental frequency

are not considered here, given that their amplitudes are extremely small and correspondingly, they are not needed to properly reconstruct the signal trace.

As prior work has shown, the relevant measurement quantity for T-MOKE ellipsometry is the intensity difference due to the inversion of the transverse magnetization, normalized by the average intensity $\Delta I/I$ [37]. The signal amplitude that is associated with the magnetic field induced magnetization reversal of the sample is indicated in figure 1(c) with the label "ΔI" and the mean value of the measured intensity is indicated by a dashed red line and label "$\langle I \rangle$". In addition to the typical benefits of measuring a relative quantity rather than an absolute value, our analysis scheme has the advantage that second order effects that could influence magneto-optical responses [44] are eliminated, because contributions to the detected light signal from even order effects in the magnetization are removed by computing ΔI for inverted magnetization states.

Figure 1(d) represents a typical T-MOKE ellipsometry data set. The characteristic features of the signal pattern, which is the sign inversion of the measured quantity upon crossing the extinction point and two clearly identifiable peaks on opposite sides of it, are indicative of a T-MOKE effect. An exact theoretical expression exists for $\Delta I/I$, which describes the dependence of this signal quantity from angle values θ_1, θ_2 and ϕ_2 and the reflection matrix parameters. The complete derivation can be found in [37], resulting in:

$$\frac{\Delta I}{I} = 4\frac{B_1 sin^2\theta_1\, h_2 + cos\theta_1 sin\theta_1[(B_1B_3 + B_2B_4)h_3 - (B_1B_4 - B_2B_3)h_4] + \frac{1}{2}B_6}{(B_3^2 + B_4^2)cos^2\theta_1\, h_1 + sin^2\theta_1\, h_2 + 2cos\theta_1 sin\theta_1(B_3h_3 - B_4h_4) + \frac{1}{2}B_5}, \tag{2}$$

where h_i are functions that depend on the angular orientation of QWP and P_2:

$$h_1 = \frac{cos^2(2\phi_2 - \theta_2)}{2} + \frac{cos^2(\theta_2)}{2}, \tag{3}$$

$$h_2 = \frac{sin^2(2\phi_2 - \theta_2)}{2} + \frac{sin^2(\theta_2)}{2}, \tag{4}$$

$$h_3 = \frac{sin(4\phi_2 - 2\theta_2)}{4} + \frac{sin(2\theta_2)}{4}, \tag{5}$$

$$h_4 = \frac{sin(2\phi_2 - 2\theta_2)}{2}, \tag{6}$$

and the B_i are the elements of the reflection matrix $\underline{R}$:

$$B_1 = Re(\tilde{\beta}), \tag{7}$$

$$B_2 = Im(\tilde{\beta}), \tag{8}$$

$$B_3 = Re(\tilde{r_s}), \tag{9}$$

$$B_4 = Im(\tilde{r_s}). \tag{10}$$

Additionally, there are other two parameters, B_5 and B_6, which respectively describe the imperfections of the optical elements and non-T-MOKE signals that enter the detector optically or electrically. Previous work showed that especially the false signal parameter B_6 is crucial for extremely small signal level detection, because it allows for an easy separation of true magneto-optical signals with our ellipsometric T-MOKE method, which might otherwise lead to severe data misinterpretations in conventional MOKE experiments [37]. Equation (2) can now be utilized to

fit a sequence of experimental data by utilizing $B_1 - B_6$ as fit parameters to determine the full reflection matrix of any sample under investigation.

The excellent agreement that can be achieved between experimental results and the theoretical description given by equation (2) can be observed upon comparing figure 1(d) with figure 1(e), which represents the least-squares fit to the data of figure 1(d) and which has been computed using equation (2) and the extracted fit parameters $B_1 - B_6$. The two plots are visually indistinguishable and the characteristic features of ellipsometric T-MOKE signals are present in both plots. The success of the fit function to quantitatively define the measured signal is also reflected by the high coefficient of determination R^2, shown in the bottom right corner of figure 1(e). The other key strength of the T-MOKE ellipsometry method is the fact that it is producing high relative effects of otherwise rather small MOKE signals. Specifically, here in figure 1(d), ΔI is an up to 4% effect of the total intensity I, that is facilitated by the measurement set-up and strategy used here. This big relative effect comes from the fact that most of the light that is not impacted by the T-MOKE effect is filtered out by the polarization optics.

b. Samples

Three samples have been investigated in this study. They are all nanometric films grown by sputter deposition. The first sample (S1) that we used is an epitaxial $Co_{74}Ru_{26}$ thin film with (10$\underline{1}$0) surface orientation grown by sputter deposition at room temperature in a pure 3-mTorr Ar atmosphere. To achieve good epitaxial quality and the particular crystal orientation that contains the c-axis within the surface plane and thus induces an in-plane easy magnetization axis, a specific growth sequence has been used, that is described in detail in prior work [44, 45]. Specifically, the sequence of sample S1 includes a hydrofluoric acid etched Si (110) substrate, 35 nm of Ag (110), 10 nm of Cr (211), 20 nm of $Co_{74}Ru_{26}$ (10$\underline{1}$0), and a 10 nm SiO_2 overcoat, which was deposited to avoid surface oxidation and contaminations of the magnetic CoRu layer [46]. The second sample (S2) consists of a 50 nm thick YIG layer deposited on a thermally oxidized Si substrate via radiofrequency magnetron sputtering and post-annealed in atmosphere at 750ºC for 1 h. On top of this layer, a 0.3 nm $Ni_{80}Fe_{20}$ layer and a 1 nm Pt overcoat have also been sputtered deposited

in succession to protect the sample [47]. The third and last sample (S3) is fundamentally the same as sample (S2) but without the $Ni_{80}Fe_{20}$ layer [47]. The layer sequences and the corresponding sample labels of all three samples are summarized in table 1. The three samples are ferromagnetic at room temperature and present a well-defined T-MOKE signal. The $Co_{74}Ru_{26}$ sample provides a higher signal and thus, S1 is used for an overview and the analysis of T-MOKE ellipsometry signal pattern as a function of the polarization state of the incident light. The two YIG films have robust ferromagnetism but produce only a small MOKE signal, so that S2 and S3 are very suitable to conduct challenging performance tests for the T-MOKE ellipsometry methodology, and especially its signal-to-noise performance.

3. Results

a. Incident light polarization analysis

The most sensitive condition for the incoming light polarization has been previously studied for the effective polarization T-MOKE detection method in [40]. In this study, it was found that an about equal mixture of s- and p-polarized light offers the best signal and performance. So, while one would expect the performance of T-MOKE ellipsometry to show a somewhat similar optimum for the incoming light polarization, this phenomenon has not been evaluated so far. This lack of knowledge is significant, given that there is a substantial difference between both methods because T-MOKE ellipsometry also determines the purely optical reflection accurately in addition to the magneto-optical signal, and thus the combined performance optimum might deviate from the one determined for the effective polarization T-MOKE detection approach. Correspondingly, we have analyzed the signal and signal-to-noise behavior of T-MOKE ellipsometry here for different incoming polarizations. Furthermore, the θ_1 dependence of equation (2) is experimentally tested for the first time, given that all prior experimental work utilized θ_1 = 45º only. Therefore, to analyze the dependence of the signal with the incident light polarization state, we measured and analyzed $\Delta I/I$ signal pattern for sample S1 for different θ_1 angles, specifically varying in the range θ_1= -10º to 100º in steps of 5º. The frequency of the applied magnetic field was 100 Hz, and its amplitude 360 Oe to ensure magnetization reversal

and even saturation along the easy axis of magnetization, which was aligned with the applied field.

For each incident light polarization angle θ_1, we first found the extinction point and subsequently conducted a full ellipsometric $\Delta I/I$ measurement of 21 x 21 (θ_2, ϕ_2) optical settings defining a $\pm$4º square grid around the extinction point. All resulting color-coded $\Delta I/I$ maps for these different θ_1 settings are represented jointly in figure 2(a). The values of QWP and P_2 that define the extinction point (${\theta_2}^{ext}$, ${\phi_2}^{ext}$) vary with θ_1 and it is this extinction point change that leads naturally to the shifted placements of the different experimental maps in figure 2(a). The θ_1 values for individual maps in figure 2(a) are marked with labels for every second map. In figure 2(a), one can also see that there are two seemingly independent color map series, to which we refer here as top-left and bottom-right series. The existence of these two different series is a consequence of the 4 different angles ϕ_2 at which the QWP can be oriented to generate linearly polarized light from any incoming elliptically polarized light. The 4 ϕ_2 angle orientations are hereby represented by two pairs, namely ${\phi_2}^{ext}$ and ${\phi_2}^{ext'}$ and the corresponding values shifted by 180º, i.e., ${\phi_2}^{ext} + 180º$ and ${\phi_2}^{ext'} + 180º$. For the polarizer P_2 there are two angular orientations θ_2 to subsequently facilitate extinction with a difference of 180º. For both data map series that are represented in figure 2(a), the angular orientation of P_2 for obtaining extinction is in the same 180º range. Meanwhile, an alternating QWP orientation from ${\phi_2}^{ext}$ to ${\phi_2}^{ext'}$ has been chosen to generate both measurement branches for subsequent θ_1 orientations. To be able to represent all the individual maps in the same figure 2(a), two vertical axes of different QWP values are utilized, one for each series. The top-left series is formed by the color-coded $\Delta I/I$ maps corresponding to incident light polarizations P_1 in the range of θ_1=-10º to 100º with a step size of 10º, while the bottom-right series corresponds to maps with P_1 values starting at θ_1=-5º and finishing at θ_1= 95º, also using a step size of 10º. As one can see, in both series the pattern intensity increases for intermediate θ_1 angle values, while it is minimal near the end points of both θ_1 map series. The variation in the pattern intensity indicates that there is a very pronounced signal dependence with the θ_1 angle.

In comparison to our experimental data in figure 2(a), figure 2(b) represents the theoretically expected $\Delta I/I$ signal according to equation (2). All individual maps represented in figure 2(b) are computed by using just one set of values for the reflection matrix. As one can see, not only are the typical features of all our T-MOKE measurements very well represented by the theoretical maps, but also the positions of their respective extinction points are properly replicated. It is hereby noteworthy that the positions of the maps do not depend on the magneto-optical properties of the sample, but only on the polarization orientation of the incident light, that is, on the θ_1 value in conjunction with the purely optical sample properties. This, in turn visualizes very clearly the ability of T-MOKE ellipsometry to measure purely optical properties with a high degree of accuracy, in addition to magneto-optical characteristics. Moreover, the pattern intensity for the different maps is also replicated with high precision.

The ellipsometric T-MOKE patterns in figure 2(a), which appear absent for $\theta_1 = 0º$ or 90º, show maximum strength for intermediate P_1 orientations. The signal disappearance when approaching pure p- or s-polarization for the incident light is predicted for our polarization sensitive ellipsometric set-up, because when having pure p- or s-polarized light, no polarization axis rotation or ellipticity change happens upon reflection. Although for pure p-polarized light, there is a T-MOKE effect that impacts the reflected light intensity, the polarization state is not actually changed [37]. Therefore, the $\Delta I/I$ signal for such incoming polarization conditions is near zero in our set-up, which is designed to detect magneto-optically induced polarization changes, and not mere reflectivity changes. To quantify the overall θ_1 dependence of the $\Delta I/I$ signal, the maximum absolute $\Delta I/I$ signal that is detected in each of the experimental maps is shown as a function of θ_1 in figure 2(c). The highest $\Delta I/I$ signal is found to be very close to a θ_1 value of 45º. The exact angle of the highest signal is sample dependent, and it is not necessarily exactly 45º but always very close to it, which is the same conclusion obtained for the effective polarization T-MOKE measurement technique in [37]. Moreover, the precision with which optical parameters can be extracted from T-MOKE ellipsometry data is the highest near θ_1 = 45º because their precision is strongly influenced by the total signal level that is achieved in T-MOKE ellipsometry measurements. Therefore, using an incoming polarization of 45º, representing an

equal combination of s- and p-polarized light, is generally the most sensible experimental choice. Correspondingly, all subsequent measurements were conducted using θ_1 = 45º.

b. Signal-to-noise performance of different Fourier components

As mentioned previously, the signal amplitude ΔI in our here implemented detection approach is reconstructed from the filtered Fourier components, specifically $\Delta I = 2(A_\omega - A_{3\omega} + A_{5\omega} - A_{7\omega})$, with $A_{i\omega}$ being the ith harmonic order amplitude of the fundamental magnetic field frequency ω in the Fourier series expansion of the measured time-dependent intensity signal trace $I(t)$ [37]. So, to understand the noise level and signal-to-noise performance of our T-MOKE ellipsometry measurements, it is meaningful to analyze the noise performance of the individually contributing frequency components. Moreover, for multilayer systems, different Fourier components do not necessarily provide the exact same information but can actually be utilized to distinguish layers [17]. Thus, there is an added value in investigating the Fourier component performance in addition to understanding the compounded performance of ΔI only. This analysis has been done for data measured on sample S2, given that its signal is rather low, making it a more challenging test case and thus more suitable for studying the sensitivity and noise aspects of T-MOKE ellipsometry in detail. Specifically, for these measurements and subsequent Fourier component analysis, we utilized an AC magnetic field of 70 Hz and an amplitude range of 135 to 315 Oe. We verified these conditions to be sufficient to ensure magnetization reversal and even saturation for this specific sample.

Figure 3 displays in the top row, the map corresponding to the total reconstructed signal $\Delta I/I$ in figure 3(a) and the experimentally detected individual Fourier component signals as $A_{i\omega}/I$ maps (figure 3(b-e)) for a magnetic field amplitude of 135 Oe. The bottom row of figure 3 shows the corresponding least-squares fits according to equation (2) in direct comparison to the data. The characteristic pattern of a T-MOKE signal is present in all maps, while at the same time, we observe a very substantial decrease of the signal amplitude for the higher frequency components. The occurrence of relevantly larger noise for the higher frequency components is not evident from the color-coded maps, which are visually identical, even if the signal is

significantly smaller for increasing i, decreasing by about an order or magnitude from i = 1 to i = 7. The values for R^2 of the least-squares fits to equation (2) are shown in the lower right corner of each bottom row subfigure. They all have values larger than 0.993, which confirms the visual impression of the maps, that the noise level of our data is very low in general and systematic deviations between data and equation (2) are seemingly non-existent.

Figure 4(a) shows the values of the optical parameters obtained for the fits displayed in figures 3(f-j), namely, the real and imaginary part of $\tilde{r}_s$. They are basically identical for all frequency components and the total $\Delta I/I$ signal, as they should be, given that all the different frequency components are measured for the same sample, and are actually measured synchronously upon sinusoidal field excitation. Thus, the pure optical information obtained from the individual frequency signals and the total reconstructed signal has to be the same in a properly functioning measurement system. Correspondingly, the fact that the optical parameters do not change with the frequency confirms the viability of the T-MOKE ellipsometry method to detect optical constants precisely.

As one can see in figure 3, the signal intensity itself decreases with the frequency of the Fourier component $i\omega$. This is unsurprising, given that the signal pattern is rather similar to a square wave, for which signal contributions to the total signal get lower with i. To extend our quantitative analysis, we can now fit equation (2) to each frequency component independently, as represented in figure 3(g-j), and determine the $\tilde{\beta}$ fit parameter for each $i\omega$ contribution separately in the formally identical way as for the $\Delta I/I$ signal analysis. Fundamentally, the $\tilde{\beta}_{i\omega}$ values can be defined for each $i\omega$ contribution as $\tilde{\beta}_{i\omega} = \tilde{\beta} \cdot m_{i\omega}$, with $m_{i\omega}$ being the normalized magnetization reversal contribution at frequency $i\omega$. This relation in between the magneto-optical frequency components and the magnetization dynamics is valid due to the fact that the *m* vs. time *t* evolution exhibits time-reversal symmetry under sufficiently large field excitation [17]. Figure 4(b) displays the measurement extracted $|\tilde{\beta}_{i\omega}|$ values for $\Delta I/I$ and $A_{i\omega}/I$, as data points, which were obtained from the least-squares fits represented in figures 3(f-j), and which show the expected substantial decrease for higher frequencies. For a perfectly square signal, corresponding to a ferromagnetic sample with only two possible magnetization states and an

infinitely fast reversal, the relation between the amplitudes of the Fourier components would follow the solid line shown in figure 4(b). The data differ slightly from this perfect square-wave behavior because the real signal is not perfectly square, but is instead weakly "trapezoidal" due to the finite slope when changing the magnetization state, as can be seen in figure 1(c). Repeating the corresponding calculations for the Fourier components while assuming that the magnetization inversion process is not instantaneous but instead requires 4% of each period to reach full saturation, results in the dashed line shown in figure 4(b), which is in very good quantitative agreement with the experimental data points. Correspondingly, we have a precise quantitative understanding of the Fourier component data in figure 3.

Figure 4(c) represents the experimentally estimated signal-to-noise ratio values SNR_e for the total reconstructed signal $\Delta I/I$ and the different Fourier components, which we define here as the quantity $|\tilde{\beta}_{i\omega}|/\sigma_{|\tilde{\beta}|}$ with $\sigma_{|\tilde{\beta}|}$ being the associated sigma confidence value of $|\tilde{\beta}_{i\omega}|$ that is obtained from the least-squares fit analysis of equation (2) to the data represented in figure (3). The so-defined SNR_e -values are one relevant indicator for the quality of the T-MOKE ellipsometry technique, our tool and the signal filtering process that we utilize. The highest value of SNR_e corresponds to the first Fourier component. Additionally, it is noteworthy that even if the signal reduces very substantially for higher Fourier components, as shown in figure 4(b), the SNR_e values stay very high, with reductions of only 10% occurring. Therefore, the SNR_e data appear to indicate that the estimated noise level is reducing almost proportionally with the signal level for higher Fourier components, making them most valuable for our measurements and subsequent data analysis. This implies that the general approach of adding these different frequency components to reconstruct $\Delta I/I$ after noise filtering is justified, as no substantial noise is added in the reconstruction process.

Furthermore, the data analysis allows us to determine the false signal contribution of every measurement, which is included in the analysis as parameter B_6 in equation (2). The fact that false signals can be accurately determined and distinguished from the real signal is an important feature of T-MOKE ellipsometry and was demonstrated in prior work [40]. However, the existence of a false signal still has a negative impact because it increases the overall signal

and thus noise level, even if average false signals can be efficiently removed from the data by fitting parameter B_6. Therefore, it is important to analyze the false signal size and investigate its impact on the different frequency components. Figure 5 represents the B_6 values for the $\Delta I/I$ signal (black symbols), and the $A_{i\omega}\ /I$ Fourier components (color symbols) for 4 different applied magnetic field amplitudes. Here, one observes a clear dependence on the applied field amplitude H_0 for the fundamental frequency, with B_6 values increasing with increased H_0. In the case of the higher Fourier components, such a dependency is not present and B_6 values remain essentially constant. This suggests that this leading false signal contribution is driven directly by the magnetic field circuit, which due to its sinusoidal nature only contains the fundamental frequency. The B_6 values for the reconstructed $\Delta I/I$ signal are dependent on the false signal contribution of all the frequency components, so they increase similarly to the B_6 values of the fundamental frequency. The particular false signal in our experiments here, which is detectable but overall extremely small, namely less than 10^{-7} of the overall signal level in all cases, is associated with a weak electrical coupling from the field excitation circuit into the signal detection electronics. Although the detector circuit is fully decoupled from the excitation circuit in our set-up, their cable cross talk is not zero. The fact that our T-MOKE system is able to identify this small magnet circuit induced false signal confirms the high sensitivity and low noise level of our system, compared to other MOKE systems that would not be able to record this minute false signal level. In any case, it is crucially important to separate the electrical field driving circuit and the photodiode electrical circuit very well, especially if high magnetic fields are needed for a particular measurement. Moreover, it is very good to see that the higher frequency B_6 values are not impacted by H_0, which reiterates their significant experimental value, even if their actual amplitudes are small.

c. Measurement sequences and repeatability analysis

The experimental grid that is used in any specific measurement sequence is defined by particular combinations of angles θ_2 and ϕ_2. The grid used so far in this work covers 21 x 21 (θ_2, ϕ_2) equidistant settings in an angular range of ±4º and thus defines a square grid, which was also

used in prior works [17, 37]. The square grid has been used for simplicity, but the specific measurement grid is not actually optimized or formally justified. It is a priori not clear, which data set is the most precise or efficient to make accurate T-MOKE ellipsometry measurements. Thus, it makes sense to explore other grid layouts and compare the results to the so far utilized (θ_2, ϕ_2) square grid. This type of analysis was done for GME measurements, and a (θ_2, ϕ_2) diagonal grid was found to exhibit superior performance [41]. Thus, given certain similarities in between GME and T-MOKE ellipsometry, we try the same here and compare the conventional square grid to a diagonal grid layout. An example of measurements utilizing these two (θ_2, ϕ_2) grids is presented in figure 6, with figure 6(a) showing the results for the squared grid and figure 6(b) the corresponding data for a diagonal grid, which is chosen to be elongated along the direction of the signal sign change, in accordance with the findings of [41]. In both grid types one measures the same number of points, so that both utilize the same measurement time for the experiment, and thus can be compared directly.

Repeatability is another key aspect that allows one to analyze the quality of T-MOKE ellipsometry in general and our specific set-up in particular. Thus, the repeatability of measurement results is studied for two different samples, specifically for samples S2 and S3, and for the two grid types defined above. An applied magnetic field of 135 Oe and frequency 70 Hz was used in the Fourier analysis, because it is sufficient to ensure magnetization reversal and saturation for both samples. For each case we have repeated a full T-MOKE ellipsometry measurement 100 times under nominally identical conditions. Subsequently, we analyzed each data set by fitting it to equation (2) as discussed above and studied the repeatability of the extracted quantities. In figure 7, the repeatability of the magneto-optical parameter $\tilde{\beta}$ is shown specifically for sample S2 by plotting for each measurement *n* the deviation of the individually measured value $|\tilde{\beta}_n|$ from the average value $\langle|\tilde{\beta}_n|\rangle$ normalized by the average value, using the (θ_2, ϕ_2) square grid (figure 7(a)) and the (θ_2, ϕ_2) diagonal grid (figure 7(f)). Moreover, this analysis of repeatability is done for each individual Fourier component $A_{i\omega}/I$ and not only for the total signal $\Delta I/I$, so that a very comprehensive analysis of repeatability and signal-to-noise ratio can be achieved. The first row in figure 7, i.e., figures 7(a-e), correspond to the 100 measurements using a (θ_2, ϕ_2) square grid and the second row, i.e., figures 7(f-j), to the (θ_2, ϕ_2)

diagonal grid. From these plots, it can be observed that the measurements are very repeatable and there are only rather small variations between repeated measurements, leading to standard deviations below 1% in all cases. Furthermore, figure 7 seems to indicate that both grids seem to generate data of similar repeatability, which is corroborated by a detailed quantitative analysis of the measured standard deviations. Thus, contrary to previously conducted GME experiments [41], there is no significant improvement when using a diagonal grid. The reason for this seems to be that all relevant information of the T-MOKE ellipsometry pattern is equally well contained within both the square and the diagonal maps, whereas for the case of GME data sets, the $\Delta I/I$ pattern show a much more elongated structure, making the diagonal grid clearly superior [41].

For the different Fourier components represented in each sub-figure in figure 7, the deviation of each individual $|\tilde{\beta}_n|$ from the average, and accordingly the standard deviation (red dashed lines), increase with the order of the Fourier component. This deterioration of higher order performance is more clearly observed in figure 8, which displays the standard deviation of $|\tilde{\beta}_n|$ divided by its mean value $\sigma_{|\tilde{\beta}_n|}/\langle|\tilde{\beta}_n|\rangle$ for the different frequency components and the reconstructed signal, with open symbols referring to square grid measurements and closed symbols to diagonal grid data. Moreover, results from two different samples (S2 and S3) are being displayed. Here, we observe only very modest changes between the values for the square and diagonal grids and furthermore, the diagonal grid is not necessarily the better performing one. Thus, no clear advantage can be associated with either grid type. In figures 7 and 8, it can also be seen, that for both samples and both grid types, the best repeatability is obtained for A_ω/I. This is consistent with the individual signal analysis of the Fourier components in figure 4(c).

It is furthermore noteworthy, that the frequency dependence in figure 8 and figure 4(c) exhibit distinct differences, given that different factors impact the two types of quantities. The contributions to the signal-to-noise performances of figure 8 and figure 4(c) come from random noise and systematic deviations. Random noise contributes to both quality indicators, while systematic deviations from equation (2) should impact primarily the quality of least-squares fits, but not the repeatability of measurements in any relevant way. Therefore, the data shown in figure 8 are not prone to systematic deviations, and only noise is relevant here. Overall, the data

in figure 8 indicate a particularly good level of performance, with $\sigma_{|\tilde{\beta}_n|}/\langle|\tilde{\beta}_n|\rangle$ values between 0.002 and 0.008, i.e. very low noise, demonstrating the quality of our methodology and tool including its signal filtering. The data in figure 8 also show a stronger frequency dependence, indicating that the relative noise level is indeed relevantly impacted by the lower signal level at higher frequencies. Looking at figure 4(c), this noise effect is basically not visible given that the biggest overall contributor to the here-determined SNR_e values are systematic errors, while the actual random noise level is relevantly smaller as shown by a quantitative comparison of the data in figures 4(c) and 8, for which $\sigma_{|\tilde{\beta}_n|}/\langle|\tilde{\beta}_n|\rangle$ values of 0.002 would correspond to SNR values of 500 following the definition used in conjunction with figure 4(c). So, even if the data collected for figure 4(c) are affected by both noise and systematic deviations, the impact of systematic variations dominates the overall behavior. Thus, the real noise impact for the different frequencies is overshadowed by systematic deviations of the fit itself, even if those are themselves very small, and the actual noise impact is only truly visible in figure 8. Last, but not least, it should be mentioned that the signal-to-noise performance of these measurements is excellent, even though we utilized samples with rather small T-MOKE relative intensity changes of the order of 10^{-4}, thus corroborating the excellent sensitivity and quantitative accuracy of T-MOKE ellipsometry.

4. Conclusions

In this work, we have demonstrated that the sensitivity of T-MOKE ellipsometry measurements is at its peak when using a balanced s- and p-polarization composition as incident linearly polarized light, a result that is very similar to the conclusion that was reached for the effective polarization T-MOKE technique [37]. In addition, we demonstrate for the first time that the T-MOKE ellipsometry fit function, i.e. equation (2), is capable of replicating experimental data for any s-p combination of the incoming light extremely well, including the typical T-MOKE signal features and the location of extinction point positions.

Contrary to previously conducted GME experiments [41], we do not find any systematic improvement for T-MOKE ellipsometry if we change the measurement grid of the optical element

settings from a square grid to a diagonal one. Instead, the two grid layouts generate equally good results, so that there is no relevant reason to move away from the so far utilized square grid in T-MOKE ellipsometry measurements, even if it is certainly possible that yet other more suitable grid types exist.

Noise and systematic deviations are characterized in detail and were observed to be below 1% for the all analyzed Fourier components of the measured signal, even when using samples that produce only a small T-MOKE signal. The impact of real noise is clearly visible in our repeatability study, which demonstrated variations of less than 0.002 and thus SNR values of better than 500 for the fundamental frequency. We furthermore observe that the higher frequency components exhibit a significantly larger relative noise level, which is expected due to the fact that their amplitude is reduced by up to a factor of 10. Nonetheless, the true SNR value of even the 7^{th} order signal stays above 100. The complementary SNR_e analysis based upon achieved fit quality shows instead a somewhat different picture, namely showing overall smaller SNR values and a much-reduced frequency dependence. This indicates that this fit-based analysis is significantly impacted by systematic deviations, even though the fit quality is excellent and the fit pattern are almost completely identical to the experimental data sets. Thus, this fit quality limit must be associated with the overall very high SNR levels that our measurement system produces, even though we especially selected samples with small T-MOKE signals. This verifies the overall very high quality of our set-up and the excellent experimental capabilities of T-MOKE ellipsometry in general.

Due to experimental limitations, electrical driving circuits can couple into the electrical detection circuit and create false signals. While those false signals ought to be minimized in experimental set-ups and are in fact demonstrated here to produce only an extremely small false signal level in our tool, it is important to point out that T-MOKE ellipsometry offers two very effective ways, by which this false signal can be separated from the real signal. The first way is by means of equation (2), because false signals do not follow the optical element configuration dependence that a true T-MOKE effect exhibits and secondly, higher harmonics are not, or far less affected by false signals and thus, they offer another way of circumventing associated detection problems in case of ultrasmall real signal levels.

Acknowledgements

Our work was supported by the Spanish Ministry of Science and Innovation under the Maria de Maeztu Units of Excellence Programme (Grant No. CEX2020-001038-M) and Project No. RTI2018-094881-B100 (MCIU/Feder), as well as by Predoctoral Fellowship No. PRE2019-088428. C. M. V. acknowledges the Basque Government for fellowship No. PRE_2021_1_0056. Sample fabrication work was supported by PRESTO-JST (JPMJPR15R8), Spin Research Network of Japan, and the Thermal and Electric Energy Technology Inc. Foundation.

Captions

Table 1:

Sample labels and corresponding layers sequences of the three samples utilized in this study.

Figure 1:

(a) Schematic of an experimental set-up for T-MOKE ellipsometry detection consisting of laser source, first polarizer (P_1), quarter wave plate (QWP), second polarizer (P_2) and photodetector. The angles θ_1, ϕ_2 and θ_2 of the optical elements are defined as the angle of their principal axis with respect to the s-polarization orientation and positive values are associated with the counter-clockwise rotation sense along the light propagation direction, as indicated by the blue arrows. The sample under investigation is located inside the gap of an electromagnet that produces a magnetic field transverse to the plane-of-incidence. The path of the laser light is indicated in the figure by red arrows. (b) AC magnetic field H vs. time t generated with our experimental control system; (c) photo-detector voltage signal I vs. time t measured on sample S1 (see table 1). The intensity $\langle I \rangle$ represented by a dashed red line is the mean value of the photo-detector voltage. ΔI is the variation in intensity due to magnetization reversal. The measured signal is shown as a grey line, while the blue curve represents the reconstructed signal. (d) Color-coded map representing experimental $\Delta I/I$ values from the reconstructed signal as a function of the QWP and P_2 angles, ϕ_2 and θ_2, respectively. (e) Color-coded map representing the $\Delta I/I$ values obtained from the fitting of (d) to equation (2); the R^2 value of this fit is displayed in the bottom right corner. The color-code that is identified on the right side of (e) applies to both (d) and (e).

Figure 2:

Color-coded maps, representing (a) the measured $\Delta I/I$ signal as a function of the QWP angle ϕ_2 and the P_2 angle θ_2 for sample S1; each independent square corresponds to a different

polarization state of the incident light, given by the P_1 angle θ_1. The corresponding values of θ_1 are labeled for every second map only, with the unindexed maps representing intermediate θ_1 values. There are two series of color-coded maps, which differ in the orientation of the QWP; the top-left series corresponds to the ϕ_2 angles represented by the left blue axis, the bottom-right series to the right orange axis. Both series share the same θ_2 axis. (b) The corresponding theoretical $\Delta I/I$ signal according to the equation (2). The color codes are identified in the bottom right corner of each subfigure and are identical. (c) Maximum experimental $\Delta I/I$ signal values vs. polarization angle θ_1, represented as black dots; the red line represents abs(sin θ_1) and is a guide to the eye.

Figure 3:

Color coded maps, representing (a-e) the experimental $\Delta I/I$ and $A_{i\omega}/I$ signals as a function of ϕ_2 and θ_2 for sample S2, and (f-j) the corresponding least-squares fits of the respective signals according to equation (2); the corresponding values of R^2 are given in the bottom right corner of each map. The color code that applies to each experimental map and the corresponding fit is displayed on the top of each column, which also provides the identifier of the quantity shown.

Figure 4:

Least-squares fit results of (a) the real and imaginary part of $\tilde{r}_s$, (b) the absolute value of $\tilde{\beta}_{i\omega}$ and, (c) the SNR_e values defined as the absolute value of $\tilde{\beta}_{i\omega}$ divided by the sigma value $\sigma_{|\tilde{\beta}|}$ obtained from the fit to equation (2) for the experimental $\Delta I/I$ signal and the $A_{i\omega}/I$ components, measured for sample S2 and thus, corresponding to the data and fits represented in figure 3. Lines in (a) show the mean values of the real and imaginary part of $\tilde{r}_s$. The solid line in (b) represents the absolute values of $\tilde{\beta}_{i\omega}$ that one would expect for a perfect square signal, while the dashed line shows values that are produced by a slightly trapezoidal signal whose magnetization inversion is not instantaneous but requires 4% of each period to reach full saturation.

Figure 5:

Least-squares fit results to equation (2) of the false signal B_6 as a function of the applied magnetic field amplitude H for the experimental $\Delta I/I$ signal and $A_{i\omega}/I$ components of sample S2.

Figure 6:

Color-coded maps, representing the measured $\Delta I/I$ signals as a function of ϕ_2 and θ_2 for sample S2 for two different grids, containing the same number of total points: (a) square and (b) diagonal. The color code is identified on the right side of the figure and applies to both maps.

Figure 7:

Normalized deviation of experimental $|\tilde{\beta}|$ values from their average for 100 independent measurements for sample S2. The different columns correspond to the extracted $|\tilde{\beta}_n|$ values determined from the total $\Delta I/I$ signal and the $A_{i\omega}/I$ components. Results for two different grid types are represented: (a-e) square grid and (f-j) diagonal grid. The red dashed lines in each sub-figure indicate the standard deviation of each data series. On top of each column, the displayed Fourier component $A_{i\omega}/I$ is identified, with the first column corresponding to $\Delta I/I$. For an easy comparison, the same scale is used in all sub-figures.

Figure 8:

Normalized standard deviation of the extracted $|\tilde{\beta}_n|$ values determined from the $\Delta I/I$ signal and the $A_{i\omega}/I$ components for 100 repeat measurements on samples S2 and S3 for square and diagonal experimental grids, respectively.

Table 1

Sample label	Layer sequence
S1	HF etched Si substrate / Ag (35 nm) / Cr (10 nm) / $Co_{74}Ru_{26}$ (20 nm) / SiO_2 (10 nm)
S2	Si substrate / YIG (50 nm) / $Ni_{80}Fe_{20}$ (0.3 nm) / Pt (1 nm)
S3	Si substrate / YIG (50 nm) / Pt (1 nm)

Figure 1

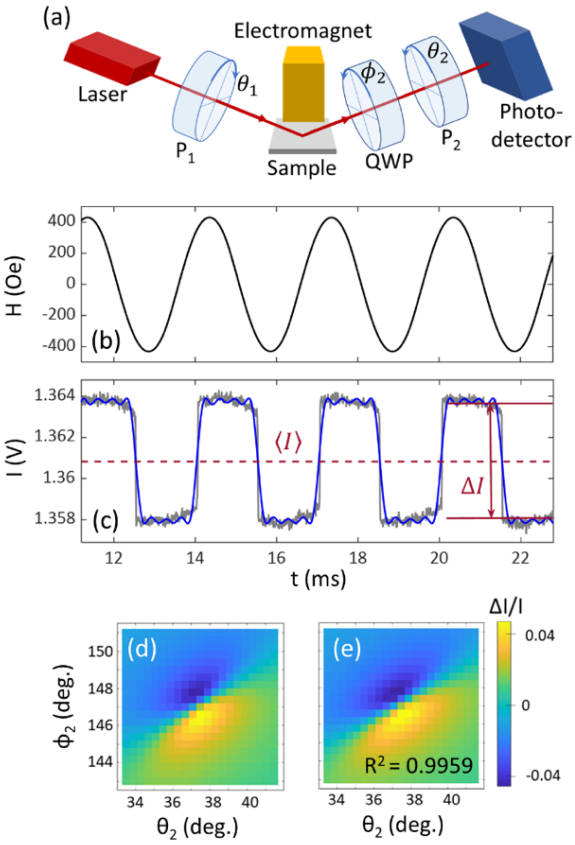
(a)
Electromagnet
Laser
θ_1
ϕ_2
θ_2
Photo-
detector
P_1
Sample
QWP
P_2
H (Oe)
400
200
0
-200
-400
(b)
I (V)
1.364
1.362
1.36
1.358
(c)
⟨I⟩
ΔI
12
14
16
18
20
22
t (ms)
ΔI/I
0.04
0
-0.04
(d)
(e)
R^2 = 0.9959
Φ_2 (deg.)
150
148
146
144
34
36
38
40
θ_2 (deg.)

Figure 2

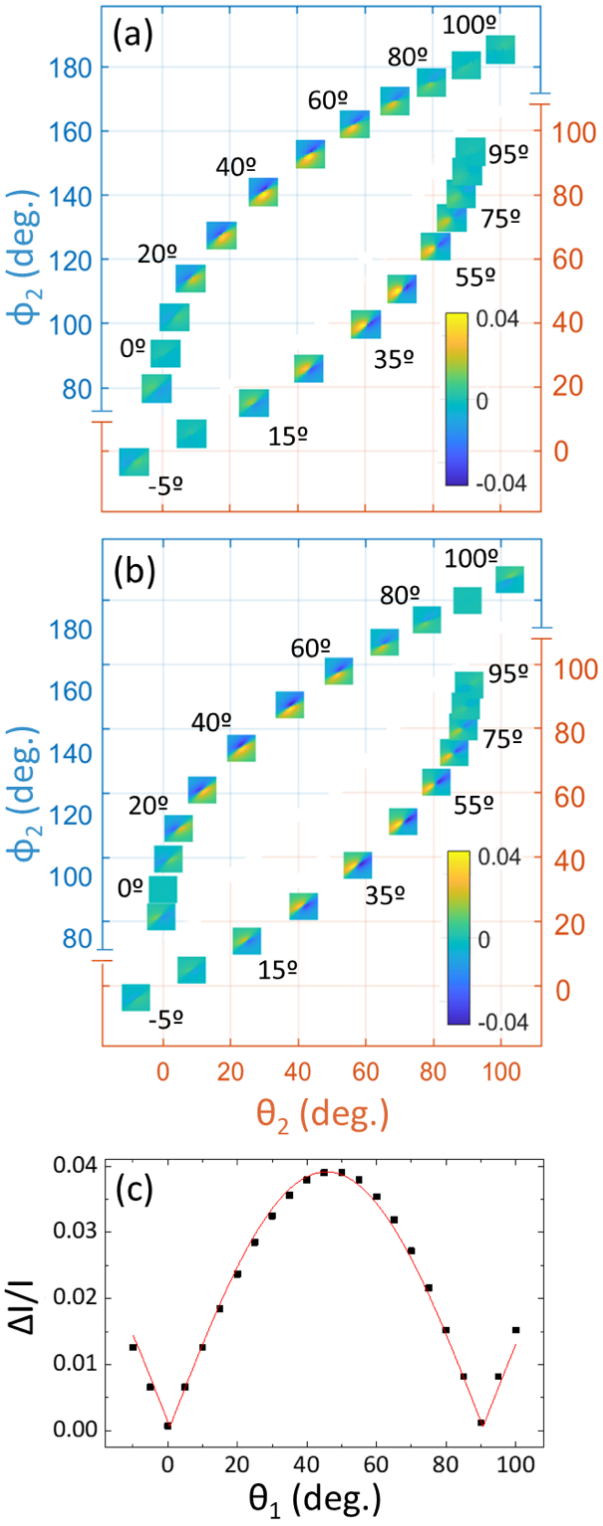
(a)
100º
80º
60º
40º
95º
75º
20º
55º
0º
35º
15º
-5º
0.04
0
-0.04
180
160
140
120
100
80
100
80
60
40
20
0
Φ_2 (deg.)
(b)
100º
80º
60º
95º
40º
75º
20º
55º
0º
35º
15º
-5º
0.04
0
-0.04
0
20
40
60
80
100
θ_2 (deg.)
(c)
0.04
0.03
0.02
0.01
0.00
ΔI/I
0
20
40
60
80
100
θ_1 (deg.)

Figure 3

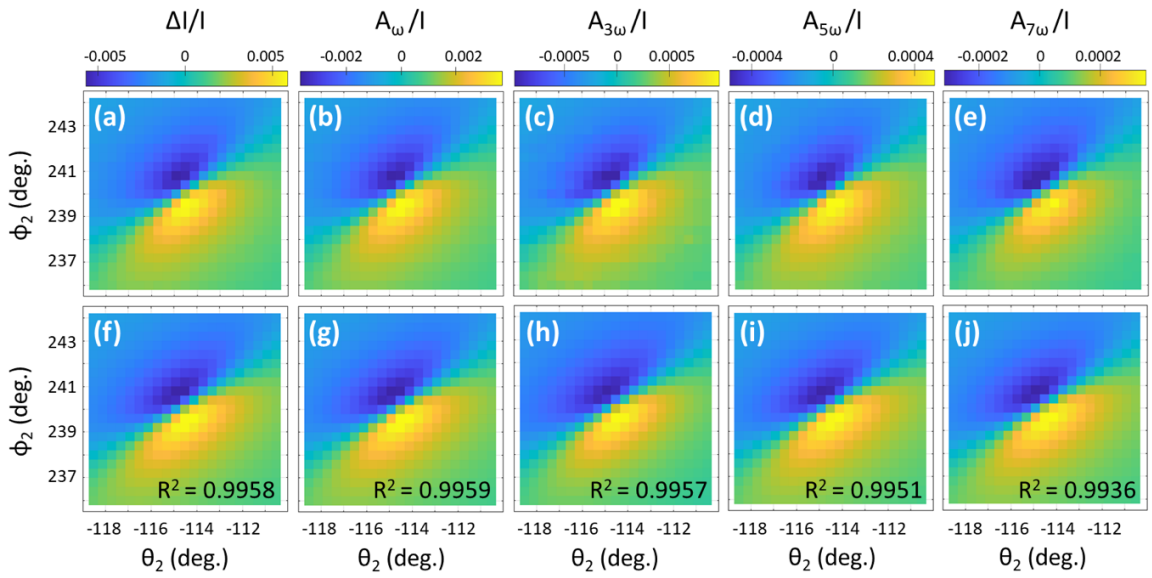
ΔI/I
A_ω /I
A_3ω /I
A_5ω /I
A_7ω /I
-0.005 0 0.005
-0.002 0 0.002
-0.0005 0 0.0005
-0.0004 0 0.0004
-0.0002 0 0.0002
(a)
(b)
(c)
(d)
(e)
(f)
(g)
(h)
(i)
(j)
ϕ2 (deg.)
243
241
239
237
R² = 0.9958
R² = 0.9959
R² = 0.9957
R² = 0.9951
R² = 0.9936
-118 -116 -114 -112
θ2 (deg.)

Figure 4

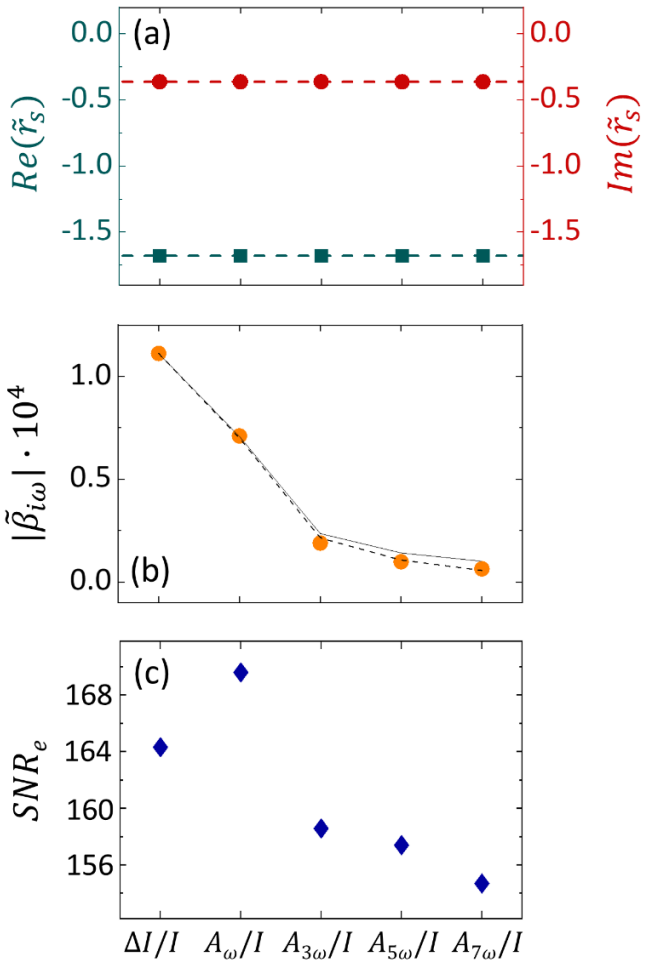
(a)
0.0
-0.5
-1.0
-1.5
$Re(\tilde{r}_s)$
$Im(\tilde{r}_s)$
(b)
1.0
0.5
0.0
$|\tilde{\beta}_{i\omega}| \cdot 10^4$
(c)
168
164
160
156
SNR_e
$\Delta I/I$
A_ω/I
$A_{3\omega}/I$
$A_{5\omega}/I$
$A_{7\omega}/I$

Figure 5

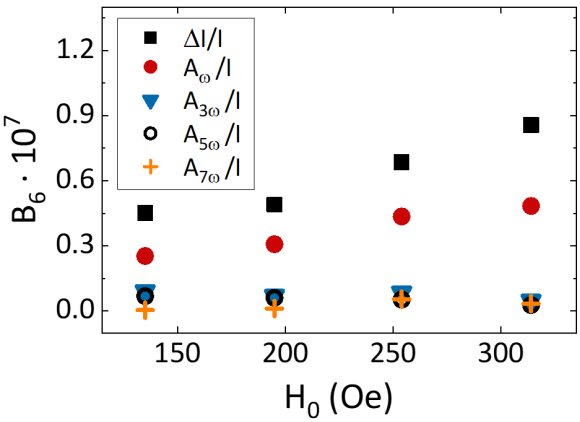
ΔI/I
A$_\omega$/I
A$_{3\omega}$/I
A$_{5\omega}$/I
A$_{7\omega}$/I
B$_6$ · 10^7
1.2
0.9
0.6
0.3
0.0
150
200
250
300
H$_0$ (Oe)

Figure 6

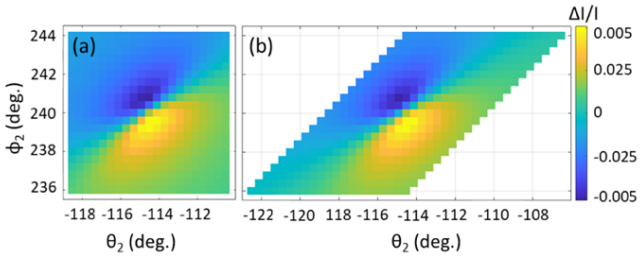
(a)
(b)
ΔI/I
0.005
0.025
0
-0.025
-0.005
244
242
240
238
236
ϕ_2 (deg.)
-118 -116 -114 -112
θ_2 (deg.)
-122 -120 118 -116 -114 -112 -110 -108
θ_2 (deg.)

Figure 7.

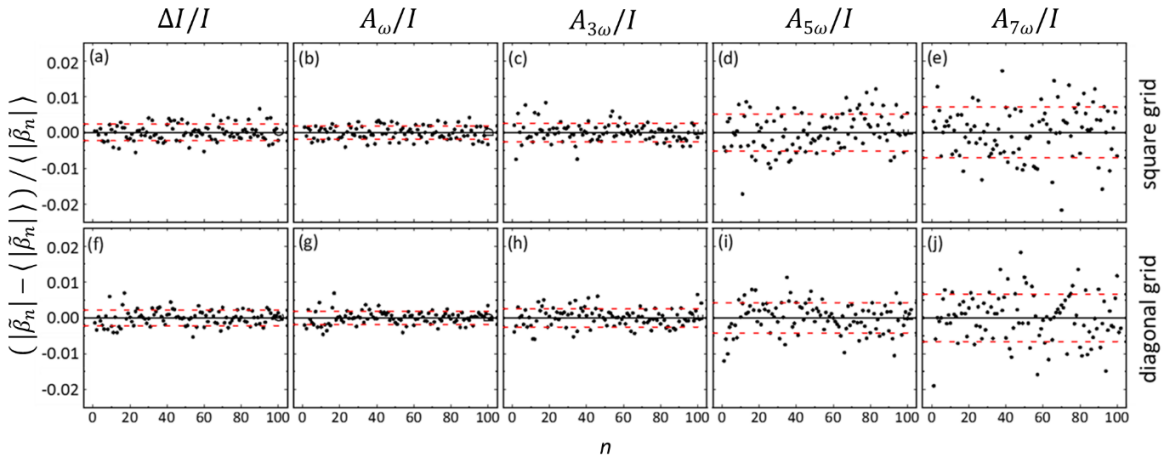
$\Delta I/I$
A_ω/I
$A_{3\omega}/I$
$A_{5\omega}/I$
$A_{7\omega}/I$
(a)
(b)
(c)
(d)
(e)
(f)
(g)
(h)
(i)
(j)
square grid
diagonal grid
$\left(|\tilde{\beta}_n| - \langle|\tilde{\beta}_n|\rangle\right) / \langle|\tilde{\beta}_n|\rangle$
0.02
0.01
0.00
-0.01
-0.02
0
20
40
60
80
100
n

Figure 8

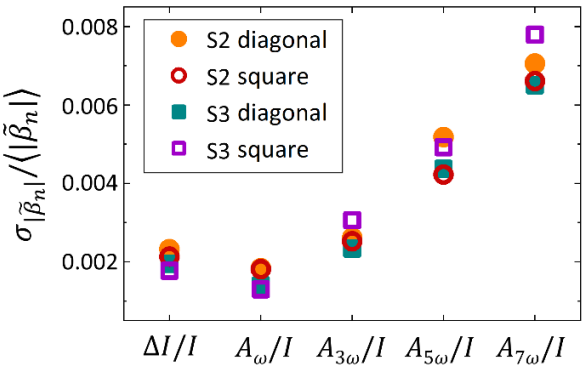
0.008
0.006
0.004
0.002
S2 diagonal
S2 square
S3 diagonal
S3 square
$\sigma_{|\tilde{\beta}_n|}/\langle|\tilde{\beta}_n|\rangle$
$\Delta I/I$
A_ω/I
$A_{3\omega}/I$
$A_{5\omega}/I$
$A_{7\omega}/I$

References

[1] Gutfleisch O, Willard M A, Brück E, Chen C H, Sankar S G and Liu J P 2011 Magnetic Materials and Devices for the 21st Century: Stronger, Lighter, and More Energy Efficient. *Adv. Mater*. **23** 821-842.

[2] Bader S D and Parkin S S P 2010 Spintronics *Annual Review of Condensed Matter Physics* **1** 71-88

[3] Bibes M and Barthélémy A 2008 Towards a magnetoelectric memory *Nat. Mater* **7** 425–426

[4] Hartmann U 2000 *Magnetic Multilayers and Giant Magnetoresistance Fundamentals and Industrial Application* (Springer-Verlag Berlin Heidelberg)

[5] Fischer P and Ohldag H 2015 X -rays and magnetism *Rep. Prog. Phys.* **78** 094501

[6] Faraday M 1846 Experimental Researches in Electricity. Nineteenth Series *Phil. Trans. R. Soc*. **136** 1-20

[7] Kerr J 1877 On rotation of the plane of polarization by reflection from the pole of a magnet *Phil. Mag*. **3** 321-343

[8] Berger A and Pufall M R 1997 Study of generalized magneto-optical ellipsometry measurement reliability *Appl. Phys. Lett.* **71** 965–7

[9] Berger A and Pufall M R 1999 Quantitative vector magnetometry using generalized magneto-optical ellipsometry *J. Appl. Phys.* **85** 4583–5

[10] McCord J 2015 Progress in magnetic domain observation by advanced magneto-optical microscopy *J. Phys. D: Appl. Phys.* **48** 333001

[11] Lau J and Shaw J. M 2011 Magnetic nanostructures for advanced technologies: fabrication, metrology, and challenges *J. Phys. D: Appl. Phys*. **44** 303001

[12] D Sander et *al*. 2017 The 2017 Magnetism Roadmap *J. Phys. D: Appl. Phys.* **50** 363001

[13] Qiu Z Q and Bader S D 1999 Surface magneto-optic Kerr effect (SMOKE) *J. Magn. Magn. Mater.* **200** 664–78

[14] Qiu Z Q and Bader S D 2000 Surface magneto-optic Kerr effect *Rev. Sci. Instrum*. **71** 1243

[15] Freiser M 1968 A survey of magneto-optic effects *IEEE Trans. Magn*. **4** 152–61

[16] Riego P et *al.* 2017 Enhanced magneto-optical Kerr effects in Py/Ag/Bi trilayers *J. Phys. D: Appl. Phys.* **50** 19LT01

[17] Martín Valderrama C et *al.* 2021 Insertion layer magnetism detection and analysis using transverse magneto-optical Kerr effect (T-MOKE) ellipsometry *J. Phys. D: Appl. Phys.* **54** 435002

[18] Beaurepaire E, Merle J-C, Daunois A and Bigot J-Y 1996 Ultrafast spin dynamics in ferromagnetic nickel *Phys. Rev. Lett.* **76** 4250–3

[19] Razdolski I et *al*. 2017 Analysis of the time-resolved magneto-optical Kerr effect for ultrafast magnetization dynamics in ferromagnetic thin films *J. Phys. Condens. Matter.* **29** 174002

[20] Stamm C et *al*. 2017 Magneto-optical detection of the spin hall effect in Pt and W thin films *Phys. Rev. Lett.* **119** 87203

[21] Gauthier D J, Narum P and Boyd R W 1986 Simple, compact, high-performance permanent-magnet Faraday isolator *Opt. Lett.* **11** 623–5

[22] Zamani M, Ghanaatshoar M and Alisafaee H 2011 Adjustable magneto-optical isolators with high transmittance and large Faraday rotation *J. Opt. Soc. Am.* B **28** 2637–42

[23] Temnov V et *al*. 2010 Active magneto-plasmonics in hybrid metal–ferromagnet structures *Nat. Photonics* **4** 107

[24] Armelles G, Cebollada A, García-Martín A and González M U 2013 Magnetoplasmonics: combining magnetic and plasmonic functionalities *Adv. Opt. Mater.* **1** 10

[25] S Tsunashima 2001 Magneto-optical recording *J. Phys. D: Appl. Phys.* **34** R87–R102

[26] Regatos D, Sepúlveda B, Fariña D, Carrascosa L G and Lechuga L M 2011 Suitable combination of noble/ferromagnetic metal multilayers for enhanced magneto-plasmonic biosensing *Opt. Express* **19** 8336–46

[27] Sepúlveda B, Calle A, Lechuga L M and Armelles G 2006 Highly sensitive detection of biomolecules with the magneto-optic surface-plasmon-resonance sensor *Opt. Lett.* **31** 1085–7

[28] Taskeya Haider 2017 A Review of Magneto-Optic Effects and Its Application *International Journal of Electromagnetics and Applications*, **7**(1) 17-24

[29] Lambert C-H et *al*. 2014 All-optical control of ferromagnetic thin films and nanostructures *Science* **345** 1337–40

[30] Verduci T et *al*. 2011 Fourier magnetic imaging *Appl. Phys. Lett.* **99** 92501

[31] Nikulina E, Idigoras O, Vavassori P, Chuvilin A and Berger A 2012 Magneto-optical magnetometry of individual 30 nm cobalt nanowires grown by electron beam induced deposition *Appl. Phys. Lett.* **100** 142401

[32] Arregi J A, Riego P and Berger A 2017 What is the longitudinal magneto-optical Kerr effect? *J. Phys. D: Appl. Phys*. **50** 03LT01

[33] Carey R and Thomas B W J 1974 The theory of the Voigt effect in ferromagnetic materials *J. Phys. D: Appl. Phys.* **7** 2362–8

[34] Hubert A and Traeger G 1993 Magneto-optical sensitivity functions of thin-film systems *J. Magn. Magn. Mater.* **124** 185–202

[35] Postava K et *al*. 1997 Linear and quadratic magneto-optical measurements of the spin reorientation in epitaxial Fe films on MgO *J. Magn. Magn. Mater.* **172** 199–208

[36] Osgood R M, Bader S D, Clemens B M, White R L and Matsuyama H 1998 Second-order magneto-optic effects in anisotropic thin films *J. Magn. Magn. Mater.* **182** 297-323

[37] Oblak E, Riego P, Garcia-Manso A, Martinez-de-Guerenu A, Arizti F, Artetxe I and Berger A 2020 Ultrasensitive transverse magneto-optical Kerr effect measurements using an effective ellipsometric detection scheme *J. Phys. D: Appl. Phys.* **53** 205001

[38] Girón-Sedas J A, Mejia-Salazar J R, Moncada-Villa E and Porras-Montenegro N 2016 Enhancement of the transverse magneto-optical Kerr effect via resonant tunneling in trilayers containing magneto-optical metals *Appl. Phys.Lett.* **109** 033106

[39] Hunt R P 1967 Contrast enhancement of the transverse Kerr effect *J. Appl. Phys.* **38** 1215

[40] Oblak E, Riego P, Fallarino L, Martinez-de-Guerenu A, Arizti F and Berger A 2017 Ultrasensitive transverse magneto-optical Kerr effect measurements by means of effective polarization change detection *J. Phys. D: Appl. Phys.* **50** 23LT01

[41] Arregi A J, Gonzalez-Diaz B, Bergaretxe E, Idigoras O, Unsal T, and Berger A 2012 Study of generalized magneto-optical ellipsometry measurement reliability *J. Appl. Phys.* **111** 103912

[42] Sato K 1981 Measurement of Magneto-Optical Kerr Effect Using Piezo-Birefringent Modulator *Jpn. J. Appl. Phys.* **20** 2403

[43] Smolenskiĭ G A et al. 1975 Birefringence of light in magnetically ordered crystals *Sov. Phys. Usp.* **18** 410

[44] Idigoras O, Suszka A K, Vavassori P, Landeros P, Porro J M, and Berger A 2011 Collapse of hard-axis behavior in uniaxial Co films *Phys. Rev. B* **84** 132403

[45] Idigoras O, Palomares U, Suszka A K, Fallarino L, and Berger A 2013 Magnetic properties of room temperature grown epitaxial Co1−xRux -alloy films *Appl. Phys. Lett*. **103** 102410

[46] Marin Ramirez J M et *al*. 2020 Experimental exploration of dynamic phase transitions and associated metamagnetic fluctuations for materials with different Curie temperatures *Phys. Rev. E* **102** 022804

[47] Niimura T et *al*. 2020 Influence of interface layer insertion on the spin seebeck effect and the spin hall magnetoresistance of Y3F e5O12/P t bilayer systems *Phys. Rev. B* **102** 094411